

Contents

1	Theory	3
1.1	Sesquioxides	3
1.1.1	Chromium Oxide	4
1.1.2	Gallium Oxide	7
1.2	X-ray Diffraction Principles	8
1.2.1	Scattering at Lattices	8
1.2.2	X-rays	9
1.3	Heteroepitaxy	10
1.3.1	Pseudomorphic Growth	10
1.3.2	Relaxed Growth	11
2	Experimental Methods	15
2.1	Pulsed Laser Deposition	15
2.1.1	Setup	15
2.1.2	Plasma Dynamics	17
2.1.3	Segmented Target Approach	17
2.2	X-Ray Diffraction Measurement	18
2.2.1	2θ - ω -scans	18
2.2.2	ω -scans	19
2.2.3	ϕ -scans	20
2.2.4	Reciprocal Space Maps	20
2.2.5	Technical Details	22
2.3	Thermal Evaporation	23
2.4	Resistivity Measurement	24
2.5	Thickness Determination	25
2.6	Spectral Transmission	26
2.7	Further Measurement Methods	26
3	Experiment, Results and Discussion	28
3.1	Growth Window for Cr_2O_3 Deposition on Sapphire	29
3.1.1	Experiment	29
3.1.2	Oxygen Partial Pressure Variation on m -plane Sapphire	29
3.1.3	Growth Temperature Variation on m -plane Sapphire	32
3.1.4	Influence of Growth Rate on Crystal Structure	33
3.1.5	Deposition on c -, r -, m - and a -plane Sapphire	35
3.1.6	Conclusion	37
3.2	Discrete Combinatorial Synthesis for Taylored Doping	39
3.2.1	Experiment	39
3.2.2	DCS with Different Targets	39
3.2.3	Conclusion	45

3.3	Strain Analysis	49
3.3.1	Experiment	50
3.3.2	Growth Rates	54
3.3.3	Strain and Tilt for Different Orientations	54
3.3.4	Conclusion	68
3.4	Cr ₂ O ₃ Buffer Layers for α -Ga ₂ O ₃	70
3.4.1	Experiment	70
3.4.2	Comparison of <i>in situ</i> and <i>ex situ</i> grown Ga ₂ O ₃ on Chromia Buffers	71
3.4.3	Conclusion	75
	Appendices	80
	A Calculations	81
A.1	<i>m</i> -plane lattice constants	81
A.2	<i>a</i> -plane lattice constants	81
	B Figures	83
	Bibliography	89

Chapter 3

Experiment, Results and Discussion

Contents

3.1	Growth Window for Cr_2O_3 Deposition on Sapphire	29
3.1.1	Experiment	29
3.1.2	Oxygen Partial Pressure Variation on <i>m</i> -plane Sapphire . . .	29
3.1.3	Growth Temperature Variation on <i>m</i> -plane Sapphire	32
3.1.4	Influence of Growth Rate on Crystal Structure	33
3.1.5	Deposition on <i>c</i> -, <i>r</i> -, <i>m</i> - and <i>a</i> -plane Sapphire	35
3.1.6	Conclusion	37
3.2	Discrete Combinatorial Synthesis for Taylored Doping . .	39
3.2.1	Experiment	39
3.2.2	DCS with Different Targets	39
3.2.3	Conclusion	45
3.3	Strain Analysis	49
3.3.1	Experiment	50
3.3.2	Growth Rates	54
3.3.3	Strain and Tilt for Different Orientations	54
3.3.4	Conclusion	68
3.4	Cr_2O_3 Buffer Layers for $\alpha\text{-Ga}_2\text{O}_3$	70
3.4.1	Experiment	70
3.4.2	Comparison of <i>in situ</i> and <i>ex situ</i> grown Ga_2O_3 on Chromia Buffers	71
3.4.3	Conclusion	75

3.2 Discrete Combinatorial Synthesis for Taylored Doping

As described in the previous chapter, the resistivity of the Cr_2O_3 thin films shows strong dependence on thin film orientation. To improve and taylor the conductivity, it is tried to incorporate acceptors into the p -type material. The elements chosen for this are lower valent Cu^{2+} via CuO and Zn^{2+} via ZnO , because doping has already been reported in literature on c -plane sapphire with magnesium via MgO [2].

3.2.1 Experiment

As described in Section 2.1.1, Equ. (2.1) can be applied to calculate the material composition χ of the plasma plume when utilizing a Discrete Combinatorial Synthesis (DCS) target. But as mentioned before, this does not account for the finite area illuminated by the laser pulse. A simple model for including this effect can be achieved by assuming a target that has an outer composition of pure Cr_2O_3 and an inner composition of Cr_2O_3 with dopant concentration $x_{D,0}$. Simulating N randomly distributed points r_i in the range Δr around a radial laser position r_{PLD} allows the calculation of doping concentration in the plasma x_D as the mean of the N calculated compositions for each r_i . The resulting dependence of x_D on r_{PLD} is visualized in Fig. 3.11a, where a higher value of Δr results in more smeared out graphs. Those *Monte Carlo* simulations can further be approximated by a linear fit, which was done for $\Delta r = 2 \text{ mm}$ (blue dotted line in Fig. 3.11a). Henceforth, the different samples fabricated with different radial laser spot positions r_{PLD} are parameterized by the expected composition x_D calculated from this linear fit. Note that due to the small concentration of dopant, it was not possible to resolve those fractions via element sensitive measurements: Dr. Daniel Splith kindly performed Energy-dispersive X-Ray Spectroscopy (EDX) measurements that resulted in no signal for either Cu or Zn.

To fabricate doped thin films, three different PLD targets were utilized. Each target was elliptically segmented, with the outer region consisting of pure Cr_2O_3 and the inner region consisting of Cr_2O_3 with dopant concentration $c_{D,0}$:

1. $c_{D,0} = 0.01 \text{ wt.\% CuO}$, called *CuO-doped*,
2. $c_{D,0} = 0.01 \text{ wt.\% ZnO}$, called *ZnO-doped (low)* and
3. $c_{D,0} = 1 \text{ wt.\% ZnO}$, called *ZnO-doped (high)*.

For each target the DCS approach was utilized, i.e. several processes were done with fixed laser spot position during deposition, but varying laser spot position *between* processes. For each process, deposition was done on all of the 4 aforementioned substrate orientations, even though m - and a -plane samples did not exhibit any substantial conductivity. This was done to check whether the conductivity of the prismatic orientations could be improved via doping. The pulse number was 40 000 for the 0.01 wt.% targets and 30 000 for the ZnO-doped (high) target.

3.2.2 DCS with Different Targets

To investigate the growth rate, spectroscopic ellipsometry measurements were performed to determine the thickness. The according growth rates of the samples produced from the CuO-doped and ZnO-doped (low) target are depicted in Fig. 3.12. The

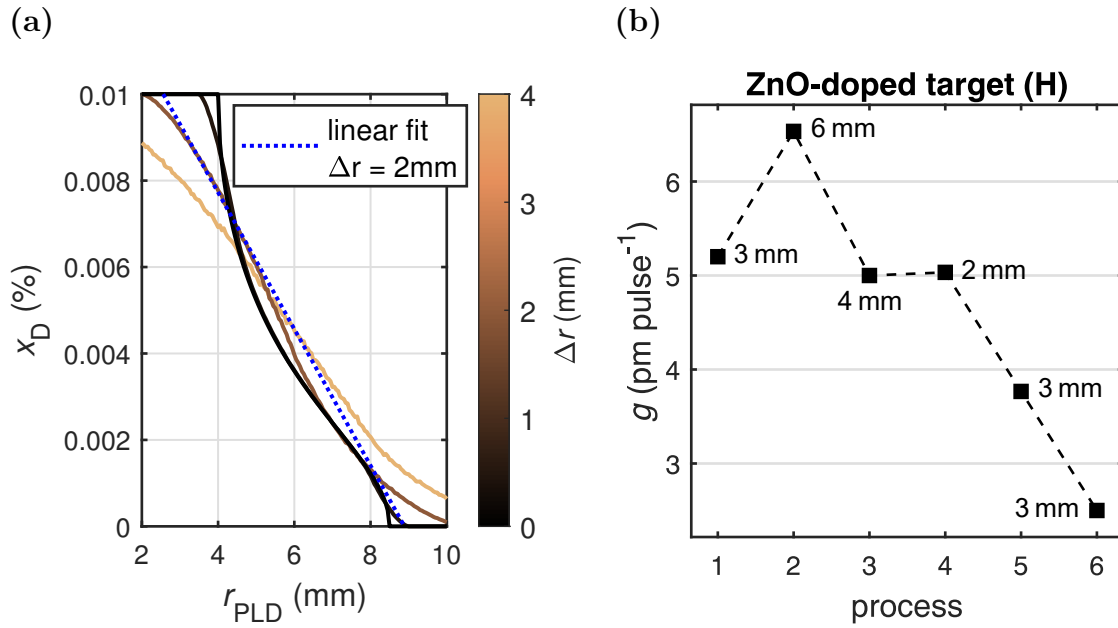


Figure 3.11: (a) Predictions for the plasma plume composition x_D using Monte Carlo simulations with $N = 10\,000$ and different values for Δr . The blue dotted line is a fit for the graph calculated with $r = 2$ mm. (b) Growth rate depending on the process order for the samples fabricated from the ZnO-doped (high) target. The laser entrance window was cleaned after each process. The applied r_{PLD} is indicated next to the marker symbols.

growth rates vary between 3 and 6 pm pulse $^{-1}$ and depend strongly on the number of deposition processes that were conducted before. By cleaning the laser entrance window after three processes, and thus reducing laser energy absorption, the growth rate is doubled, which is non-negligible. This is similar to the results obtained in chapter 3.1.

To circumvent the effect of the window blinding with each process, the window was cleaned after each process for the samples produced from the ZnO-doped (high) target. The growth rates depending on the fabrication order for the those samples are depicted in Fig. 3.11b. However, note that the growth rate still varies from approx. 2.5 to 6.5 pm pulse $^{-1}$, even though the laser entrance window was cleaned after each process. So this variation in growth rate must be traced back to another effect. Only the first sample was fabricated with 40 000 pulses, which explains the increment of growth rate between the first and second process: The condensation of material on the laser entrance window yields a decreasing growth rate over time. This has a strong effect on the overall growth rate calculated for the complete process. Furthermore, the second process was done with $r_{PLD} = 6$ mm, which is rather outside compared to the 1st, 3rd and 4th process with 3 mm, 4 mm and 2 mm, respectively. This results in a larger total ablated area and in less target degradation. Therefore, the hypothesis is that target degradation during deposition has an influence on the growth rate. To systematically investigate this, three processes were conducted at the same radius, namely process 1, 5 and 6. Note that all these samples were fabricated with $r_{PLD} = 3$ mm and otherwise the same deposition parameters. The only variation is that tracks are carved into the target by the laser (Fig. 3.13c). This is probably the reason for a crucial change in plasma dynamics and therefore a reduction of the growth rate from approx. 5 to 2.5 pm pulse $^{-1}$.

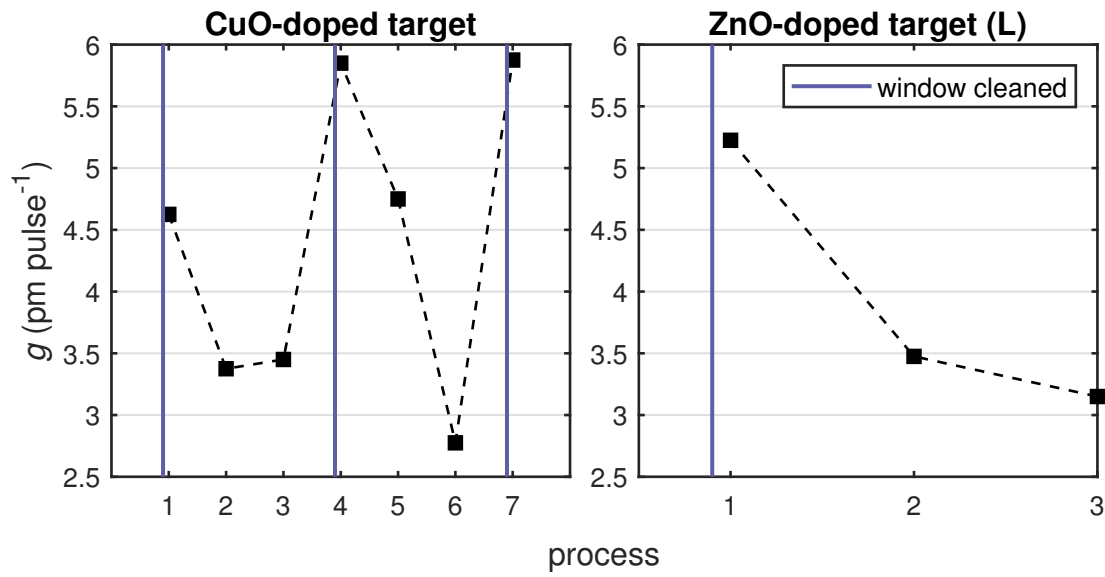


Figure 3.12: Growth rate depending on the process order for the samples fabricated from the CuO-doped and ZnO-doped (low) target. It is indicated when the laser entrance windows was cleaned.

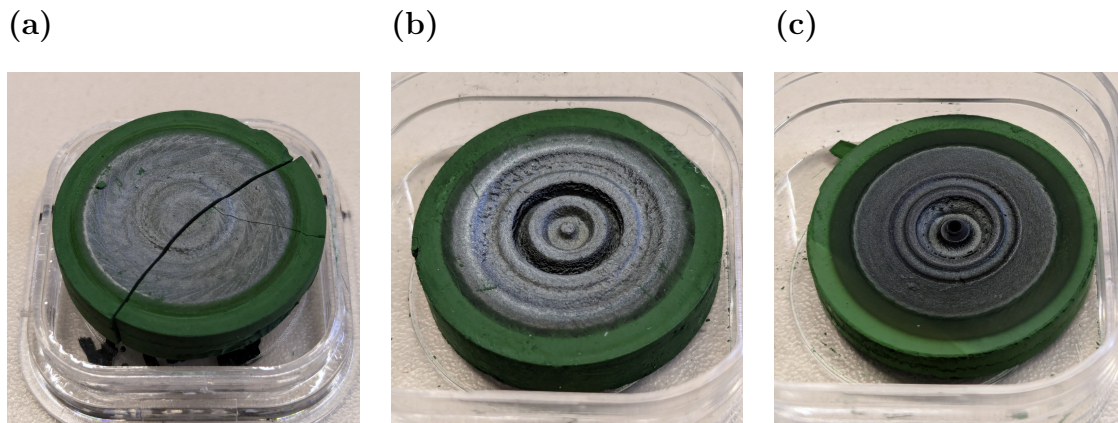


Figure 3.13: Photograph of the (a) CuO-doped, (b) ZnO-doped (low) and (c) ZnO-doped (high) target. The CuO-doped target broke during the last process it was used in. The silverish tint is presumably due to the formation of metallic chromium oxide CrO_2 on the target surface.

To probe the conductivity of the fabricated samples, resistivity measurements were performed using the PAUW methods. Only r - and c -plane samples were investigated, because the prismatic planes exhibited resistances of several $\text{G}\Omega$ or higher, when measured with a multimeter, as the HALL-effect measurement setup at the semiconductors group is not designed to measure such high resistivities. In Fig. 3.14a, the measured resistivity ρ at room temperature depending on the predicted dopant concentration x_D is depicted. From the unsystematic variation in resistivity (2 to $500\ \Omega\text{cm}$), it can be concluded that the attempt of doping the Cr_2O_3 thin films resulted in no improvement of conductivity. Using the two targets with different concentration of ZnO in the inner ellipse, no change was observed when adjusting x_D between 0.001 % and 1 %. In particular, note the aforementioned samples (1, 5 and 6 in Fig. 3.11b) that were fabricated with the same growth condition $r_{\text{PLD}} = 3\text{ mm}$, corresponding to the triangles in Fig. 3.14a at approx. $x_D = 1\%$: here, the same process parameters yield samples differing in resistivity by 2 orders of magnitude. Because those samples showed different growth rates due to target degradation, it is plausible that these altered growth dynamics also influence the conductivity.

Because in the previous chapter 3.1 it was shown that the growth rate is correlating to the ω -FWHM, Rocking scans were performed on the (00.6) and (02.4) reflection for c -plane and r -plane samples, respectively. The extracted ω -FWHMs are depicted in Fig. 3.15 depending on the growth rate for the respective process. A general trend is that the crystallinity increases for lower growth rates, namely for a growth rate of 3.4 pm pulse^{-1} , a ω -FWHM of $4'$ ($240''$) can be achieved. It is irrelevant, whether this reduction in growth rate is due to lower fluence on the laser target due to infrequent window cleaning (CuO-doped and ZnO-doped (low) target) or due to target degradation (ZnO-doped (high) target). The better FWHM is achieved for c -plane samples. Note that for the deposition of Cr_2O_3 on r -plane sapphire from the ZnO-doped (high) target, no thin film peaks in 2θ - ω -scans were observed (Fig. B.1). Those X-ray-amorphous films are presumably a result of the drastically altered plasma dynamics due to target degradation.

To investigate the influence of crystal quality on the electrical properties, in Fig. 3.14b, the resistivity depending on the ω -FWHM is depicted. It becomes clear that a higher mosaicity results in higher conductivity. Since more dislocations correspond to more crystal defects (cf. section 1.3.2), this result is in accordance to the predicted influence of crystal defects on the electrical properties of Cr_2O_3 thin films (cf. section 1.1.1). It has to be noted that this effect is less pronounced for r -plane samples compared to c -plane samples, where resistivities as low as $1.9\ \Omega\text{cm}$ can be achieved for an ω -FWHM of $40'$. Furthermore, this does not explain why m - and a -plane Cr_2O_3 exhibit such high resistivity, because their ω -FWHM is comparable to the basal and pyramidal orientations (cf. Tab. 3.1).

For each target, one c -plane sample with presumably highest doping concentration (smallest r_{PLD}) was chosen to perform temperature dependent resistivity measurements in the range of 40 to 390 K (Fig. 3.16). For all samples, an ARRHENIUS-like behavior is observed with two linear regimes above and below 100 K, respectively. By applying Equ. (3.3), two activation energies can be extracted that are listed in Tab. 3.2. Note that there is no significant difference between the undoped and doped samples. Furthermore, the samples with the smallest ablation radius for each target were chosen, and not the samples with the highest conductivity for each batch. Therefore, the data in Fig. 3.16 does not indicate that samples from the Cu-doped target have lower conductivity per se.

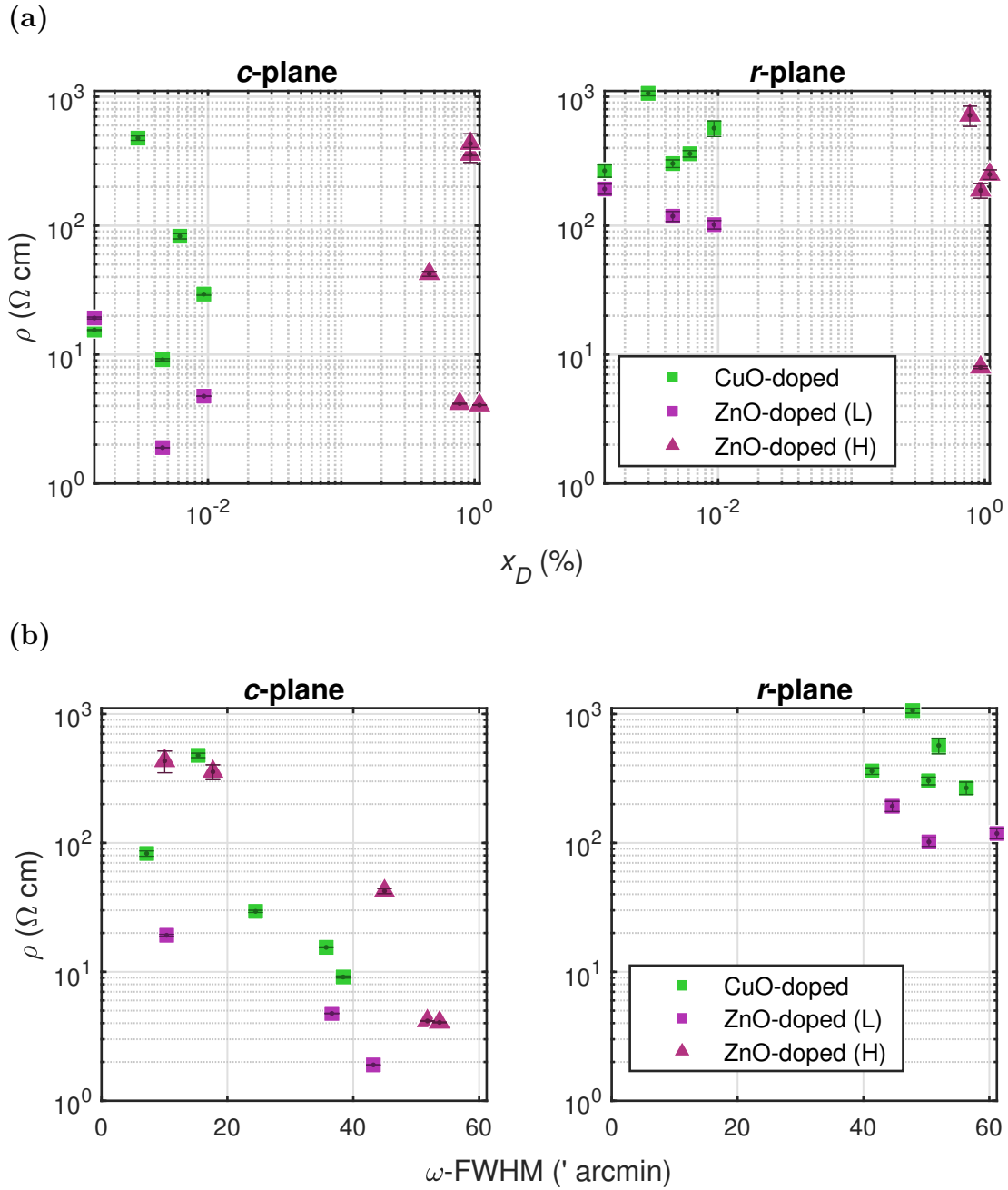


Figure 3.14: (a) Resistivity vs. predicted dopant concentration for *c*- and *r*-plane samples fabricated from all three radially segmented targets. (b) Resistivity vs. ω -FWHM of the aforementioned samples. Note that the *r*-plane samples fabricated from the ZnO-doped (high) target did not exhibit sufficient peak intensity to determine the ω -FWHM.

Table 3.2: Activation energies E_A extracted from the linear regimes in the temperature dependent resistivity measurements (Fig. 3.16).

target	E_A (meV)	
	< 100 K	> 100 K
CuO-doped	53	83
ZnO-doped (low)	35	61
ZnO-doped (high)	31	50
pure Cr_2O_3	35	54

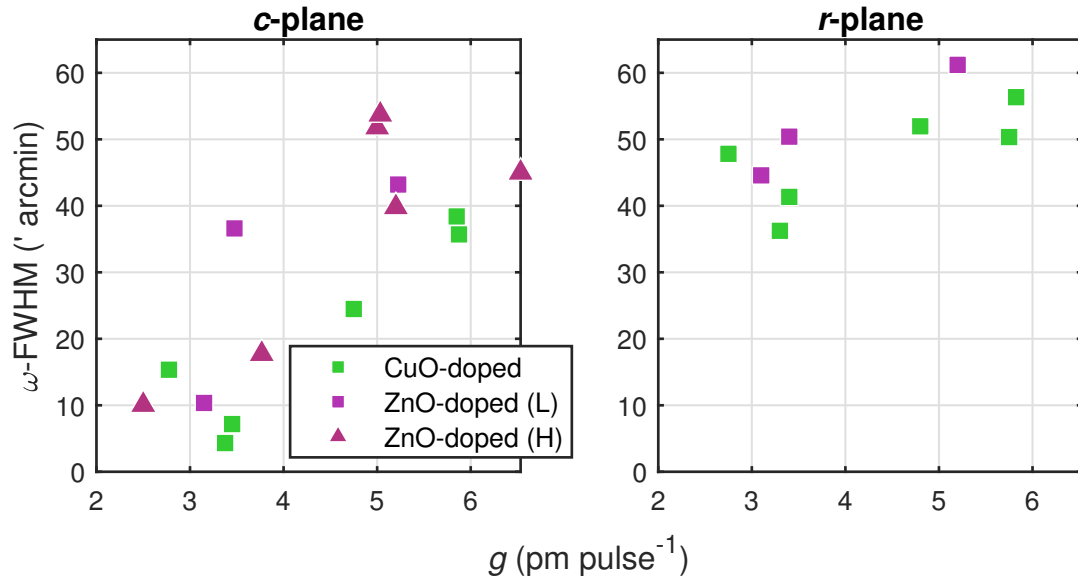


Figure 3.15: ω -FWHM for c - and r -plane samples that were fabricated from the three radially segmented targets.

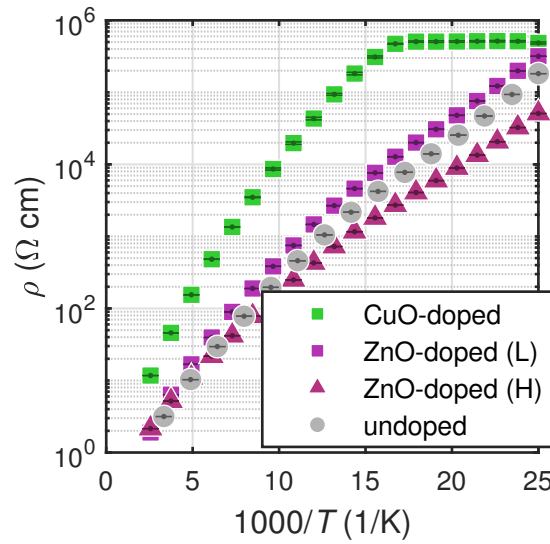


Figure 3.16: Temperature dependent resistivity measurements for c -plane samples fabricated from the different radially segmented targets, as well as a pure Cr_2O_3 target. The clipping of the sample from the CuO-doped target (green squares) is due to the limited resolution of the measurement device and the artifact nature of this saturation is confirmed by repeated measurements with different current applied during measurement (not shown).

Even though the doping resulted in no improvement of the electrical properties of the thin films, the several samples fabricated at different growth conditions – due to infrequent laser window cleaning and target degradation – may serve as an insight into the out-of-plane (o.o.p.) strain that was already observed in chapter 3.1. The o.o.p. strain dependent on the growth rate is depicted in Fig. 3.17a and was determined from Cr_2O_3 peak positions in 2θ - ω patterns. For m - and a -plane, the hypothesis of increasing strain with increasing growth rate can be confirmed. However, the slope of this relation differs depending on the target: the samples fabricated from the CuO-doped target showed less strain depending on growth rate than the samples fabricated from the ZnO-doped (high) target. This may be explained by the fact that the target degradation for the former (cf. Fig. 3.13a) was not so pronounced when compared to the latter (cf. Fig. 3.13c).

A reverse behavior is observed for c -plane samples: the strain is increasing with higher growth rates. But compared to m - and a -plane, there is no significant difference between the samples fabricated from different targets. This leads to the assumption that the plasma dynamics do not determine the o.o.p. strain for this orientation. It has to be noted that due to the constant pulse number, a change in growth rate corresponds to a change in thickness of the thin films. Therefore, it may be possible that the strain of the thin samples (low growth rate) is due to pseudomorphic growth on the corresponding Al_2O_3 substrate. Note that this leads not to the conclusion that the origin of the strain in m - and a -plane samples is also pseudomorphic growth: There, the thicker samples show more strain which is not expected because far away from the interface, dislocations should form to propagate relaxed growth. For r -plane samples, the overall strain is smaller and shows a less pronounced trend similar to m - and a -orientation. Because r -plane has both basal and prismatic character, both thickness and plasma dynamics effects may contribute to the observed strain.

The qualitative difference between c -plane and the other orientations can also be observed in Fig. 3.17b, where the ω -FWHM is shown depending on the o.o.p. strain. Compared to the previous results (cf. Fig. 3.7a), both factors characterizing crystal quality (strain and ω -FWHM) are not minimized simultaneously.

3.2.3 Conclusion

The incorporation of CuO or ZnO had no effect on the conductivity of c - and r -plane oriented Cr_2O_3 thin films. None of the m - or a -plane oriented films became conductive. However, the conductivity depends strongly on the crystallinity, which indicates intrinsic defects as the origin of charge carriers. The crystallinity is mainly influenced by target degradation due to repeated ablation with the same laser spot position on the target. This results in lower growth rates and presumably less kinetic energy of the plasma species which deposits on the substrate. Even though the doping attempt showed no effect, a discrete material library of Cr_2O_3 thin films with different strains was provided. A fundamental difference between c -plane and the other common orientations was observed, regarding the origin of the observed o.o.p. strain. Further measurements must be conducted to deconvolute the effects of (i) thickness, (ii) laser fluence on target and (iii) target degradation.

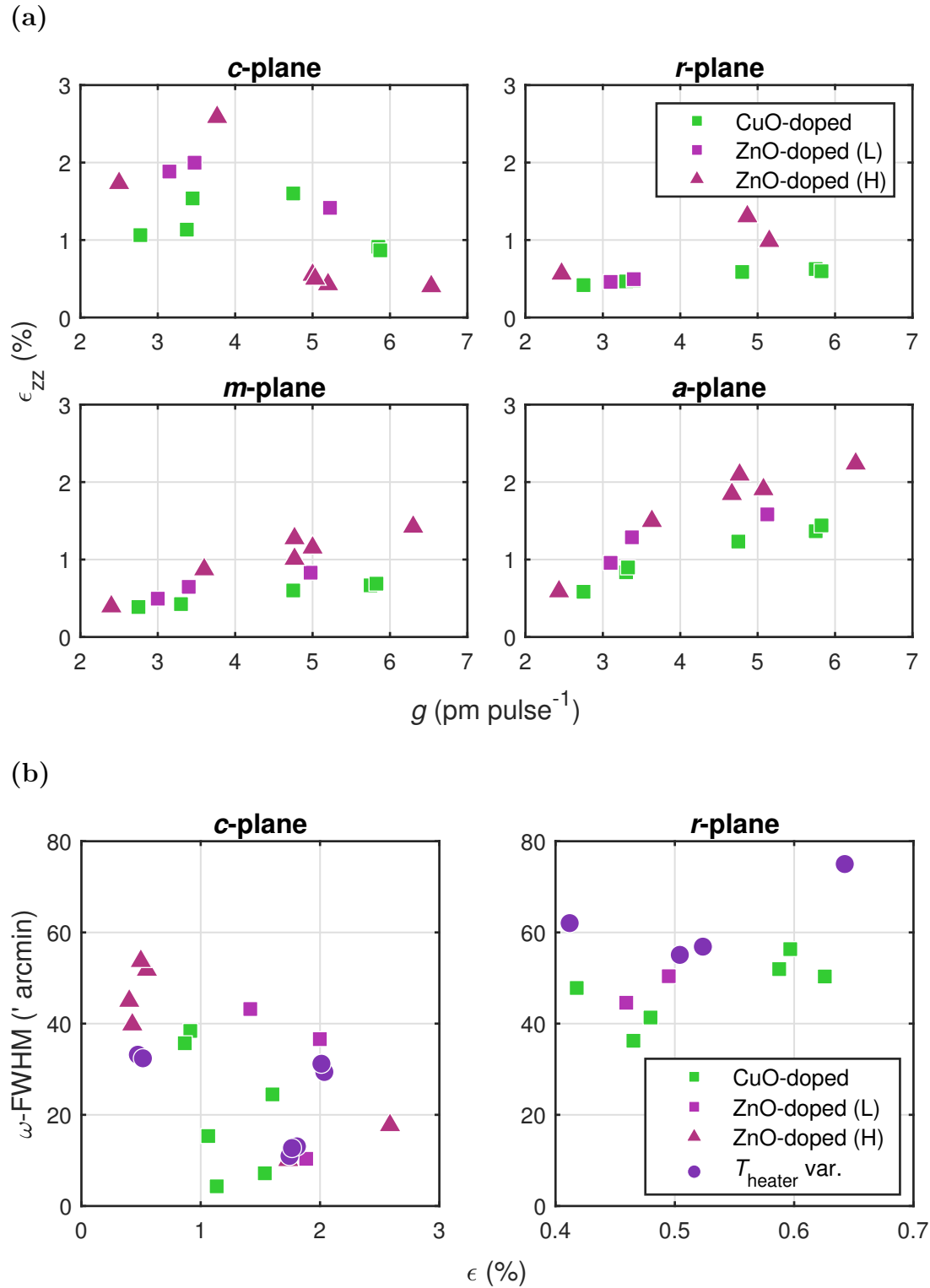


Figure 3.17: (a) Strain extracted from the peak positions in 2θ - ω -scans for samples fabricated from the three radially segmented targets. (b) Correlation between strain and ω -FWHM for *c*- and *r*-plane samples. The samples fabricated at different growth temperatures are also included.

Bibliography

- [1] Clemens Petersen *et al.* “PLD of α -Ga₂O₃ on m-plane Al₂O₃: Growth regime, growth process, and structural properties”. In: *APL Materials* 11.6 (2023), p. 061122. ISSN: 2166-532X. DOI: [10.1063/5.0149797](https://doi.org/10.1063/5.0149797).
- [2] L. Farrell *et al.* “Conducting mechanism in the epitaxial *p*-type transparent conducting oxide Cr₂O₃:Mg”. In: *Physical Review B* 91.12 (2015), p. 125202. ISSN: 1098-0121, 1550-235X. DOI: [10.1103/PhysRevB.91.125202](https://doi.org/10.1103/PhysRevB.91.125202).
- [3] Zhishan Mi *et al.* “The effects of strain and vacancy defects on the electronic structure of Cr₂O₃”. In: *Computational Materials Science* 144 (2018), pp. 64–69. ISSN: 09270256. DOI: [10.1016/j.commatsci.2017.12.012](https://doi.org/10.1016/j.commatsci.2017.12.012).
- [4] Chun-Shen Cheng, H. Gomi, and H. Sakata. “Electrical and Optical Properties of Cr₂O₃ Films Prepared by Chemical Vapour Deposition”. In: *Physica Status Solidi (a)* 155.2 (1996), pp. 417–425. ISSN: 00318965, 1521396X. DOI: [10.1002/pssa.2211550215](https://doi.org/10.1002/pssa.2211550215).
- [5] M.F. Al-Kuhaili and S.M.A. Durrani. “Optical properties of chromium oxide thin films deposited by electron-beam evaporation”. In: *Optical Materials* 29.6 (2007), pp. 709–713. ISSN: 09253467. DOI: [10.1016/j.optmat.2005.11.020](https://doi.org/10.1016/j.optmat.2005.11.020).
- [6] Max Kneiß *et al.* “Strain states and relaxation for α -(Al_{*x*}Ga_{1-*x*})₂O₃ thin films on prismatic planes of α -Al₂O₃ in the full composition range: Fundamental difference of a- and m-epitaxial planes in the manifestation of shear strain and lattice tilt”. In: *Journal of Materials Research* 36.23 (2021), pp. 4816–4831. ISSN: 0884-2914, 2044-5326. DOI: [10.1557/s43578-021-00375-3](https://doi.org/10.1557/s43578-021-00375-3).